Rare Metal Materials and Engineering
Volume 54, Issue 5, May 2025
Available online at www.rmme.ac.cn

Science Press

Cite this article as: Yang Han, Li Bo, Lu Jinwei, et al. Hot Deformation Characteristics of Fe-Cr-Ni-based Alloys in Advanced Nuclear Applications[J]. Rare Metal Materials and Engineering, 2025, 54(05): 1134-1144. DOI: https://doi.org/10.12442/j.issn.1002-185X.20240228.

ARTICLE

Hot Deformation Characteristics of Fe-Cr-Ni-based Alloys in Advanced Nuclear Applications

Yang Han[1,2], Li Bo[1,2], Lu Jinwei[1,2], Xu Long[1,2], Chen Wanqing[2,3], Zhou Wei[4], Du Yong[5]

[1] Hubei Engineering Research Center for Graphite Additive Manufacturing Technology and Equipment, China Three Gorges University, Yichang, 443002, China; [2] College of Mechanical and Power Engineering, China Three Gorges University, Yichang 443002, China; [3] Guangdong Midea Group Kitchen & Bathroom Appliance Manufacturing Co., Ltd, Foshan 528311, China; [4] School of Materials Science and Engineering, Northwestern Polytechnical University, Xi'an 710072, China; [5] State Key Laboratory of Powder Metallurgy, Central South University, Changsha 410083, China

Abstract: Thermal deformation characteristics of Fe-Cr-Ni-based alloys for nuclear power plants were investigated using a Gleeble-3500 thermal simulation tester. The microstructure evolution law of alloy heat deformation was investigated using the electron backscatter diffraction (EBSD) technique. Results demonstrate that the flow stress curves show typical dynamic recrystallization (DRX) characteristics. According to EBSD analysis, the nucleation and growth of DRX grains are mainly at grain boundaries. The complete DRX occurs at 1100 °C/0.01 s^{-1} condition, and the grains are refined. The main DRX nucleation mechanism of the alloy is the grain boundary bowing nucleation. Therefore, the softening mechanism of Fe-Cr-Ni-based alloys for nuclear power plants is the combination of dynamic recovery and DRX. The Arrhenius constitutive model with strain compensation is developed. The correlation coefficient between the predicted and experimental values is 0.9947. The reliable mathematical model of critical stress (strain) and Z parameter is obtained. The critical stress (strain) of DRX increases as the temperature decreases or the strain rate increases. The DRX kinetic model is established by the Avrami model, and a typical S-type curve is obtained. As the strain rate decreases and the temperature increases, the volume fraction of DRX increases.

Key words: Fe-Cr-Ni-based alloy; EBSD; constitutive equation; DRX

1 Introduction

With the development of the nuclear power industry, nuclear power plants are increasingly seeking breakthroughs in safety, thermal efficiency, and fuel efficiency. Therefore, stainless steel materials for nuclear power have become a hot topic of research[1–2]. Compare with 304 or 316L stainless steel, Fe-Cr-Ni-based alloy has better corrosion resistance in advanced nuclear applications due to the presence of a small amount of Cu and Si in the alloy[3–7]. Because of its good intergranular corrosion resistance, Fe-Cr-Ni-based alloys have gradually become an important reactor coolant pipeline material in advanced nuclear applications. Based on the design standards of nuclear power plants, strict requirements are put forward for microstructural stability[8–9]. Thus, Fe-Cr-Ni-based alloys in advanced nuclear applications cannot have phase transformation during heat treatment, and the grain sizes of Fe-Cr-Ni-based alloys cannot be refined by heat treatment but only through hot working[10–11]. Therefore, it is necessary to regulate microstructure and to improve comprehensive performance of Fe-Cr-Ni-based alloys in advanced nuclear applications by hot working techniques.

As is well known, metal materials undergo work hardening and dynamic softening behavior during hot deformation. Dynamic recrystallization (DRX) is the most effective softening behavior[12–14]. The comprehensive performance and microstructure characteristics of metal materials are

Received date: April 16, 2024
Foundation item: Key Projects of Hubei Provincial Department of Education (D20201206); Industrial Technology Basic Public Service Platform in 2022 (2022-232-223); National Natural Science Foundation of China (51531009)
Corresponding author: Li Bo, Ph. D., Associate Professor, College of Mechanical and Power Engineering, China Three Gorges University, Yichang 443002, P. R. China, E-mail: liboctgu@163.com

influenced by the occurrence of DRX[15–16]. Therefore, research on hot deformation characteristics of Fe-Cr-Ni-based alloys to determine the appropriate hot working parameters is very necessary for engineering application.

In recent years, many scholars have paid more attention to studying hot deformation characteristics of stainless steel. Chiu et al[17] researched hot deformation characteristics of 316 stainless steel at the deformation condition of 800–1100 °C/ 0.001–1 s^{-1}. The constitutive equation and hot processing map were constructed. It was found that the dislocation creep was the hot deformation mechanism of stainless steel. Jin et al[18] investigated static recrystallization phenomenon of 316LN ASS. By analyzing the relationship between microstructure and softening mechanism, Li et al[19] found that protrusion nucleation at the grain boundary is the primary nucleation mechanism of 300M steel. Li et al[20] found that the as-rolled 254SMo superaustenitic stainless steel was susceptible to DRX at high temperatures and low strain rates. Zhang et al[21] researched DRX behavior of 904 superaustenitic stainless steel. Zhao et al[22] plotted the hot processing map of 40CrNi by hot compression tests to determine the optimal deformation parameters. Chegini et al[23] determined the optimal thermal deformation conditions of AISI 414 stainless steel by constructing a 3D hot processing map. Therefore, detailed studies of hot deformation behavior and DRX mechanisms of Fe-Cr-Ni-based alloys in advanced nuclear applications are imperatively needed.

In this research, the hot deformation characteristics of Fe-Cr-Ni-based alloys in advanced nuclear applications were studied by hot compression tests. Electron backscatter diffraction (EBSD) was used to study microstructural characteristics. According to the experiment results, the strain-compensated Arrhenius constitutive model was constructed. The influence of deformation conditions on the volume fraction of DRX was researched by establishing DRX kinetic model. This research was expected to provide theoretical basis for the actual production of nuclear power plants.

2 Experiment

Table 1 shows the chemical composition of Fe-Cr-Ni-based alloys. Fig. 1 reveals the metallographic microstructure and X-ray diffraction (XRD) patterns of the studied Fe-Cr-Ni-based alloy before hot compression test. As shown in Fig. 1, the equiaxed grains and annealing twins can be observed. The grain size of equiaxed grains was about 100 μm. The Gleeble-3500 thermal simulator was used to perform hot compression tests. The compressed sample ends were entrapped with the lubricant during the hot compression test.

Fig. 2 shows the thorough procedure for hot compression test. After hot compression test, samples should be water quenched immediately. Fig. 3 shows a schematic diagram of microstructure characterization. The wire cutting machine was used to cut the samples for microstructure characterization, and then EBSD was used to analyze microstructure evolution during hot deformation. The metallographic corrosion reagent was aqua regia ($HCl:HNO_3$=3:1). EBSD samples were observed by TESCAN MIRA3 SEM after electropolishing. The data of EBSD analysis was studied and processed by HKL Channel 5 software to obtain the information of grain structure and size.

Table 1 Chemical composition of Fe-Cr-Ni-based alloy (wt%)

C	N	Cr	Ni	Mo	Mn	Si	Cu	Fe
≤0.015	≤0.14	15.0–18.0	10.0–14.0	2.5–3.0	1.5–2.0	≤0.32	≤0.06	Bal.

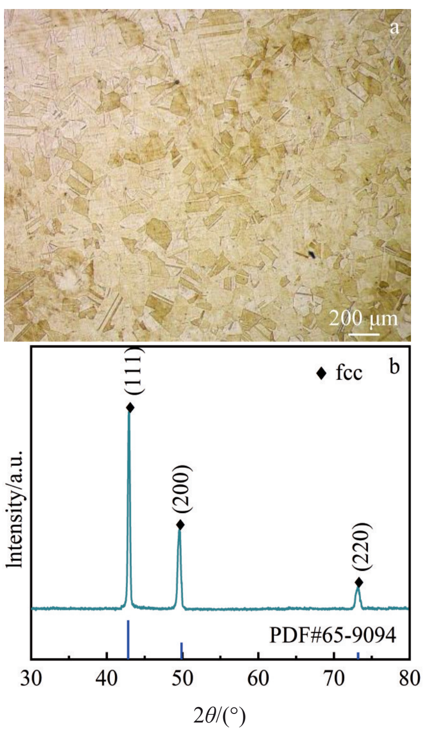

Fig.1 Microstructure (a) and XRD pattern (b) of Fe-Cr-Ni-based alloy before hot compression test

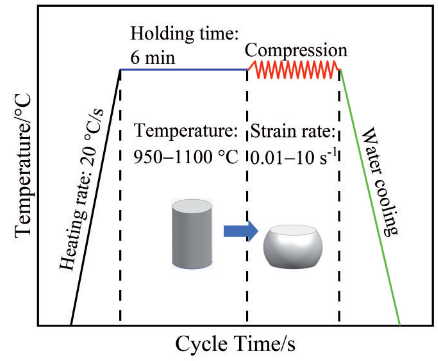

Fig.2 Experiment procedure of hot compression test

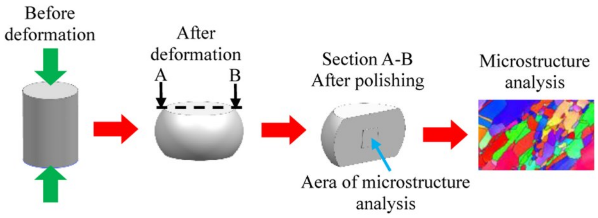

Fig.3 Schematic diagram of microstructure characterization

3 Results and Discussion

3.1 True stress-true strain curves

The true stress-true strain curves of the studied Fe-Cr-Ni-based alloy are shown in Fig.4. The flow stress increases as the strain rate increases or the temperature decreases[24–25]. There are three stages in the flow stress change trend[26]. The first stage: with the increase in strain, the flow stress rapidly increases until it reaches a maximum value in the early stage. At this stage, the internal dislocation of the studied alloy rapidly increases with strain, leading to an increase in deformation resistance and resulting in work hardening. At a constant temperature, the work hardening phenomenon becomes more obvious as the strain rate increases. The second stage: as the strain increases, the internal distortion energy of the studied alloy increases continuously. When it reaches a certain degree, dynamic recovery (DRV) or DRX occurs, and the flow stress gradually decreases as the strain increases, leading to flow softening. The third stage: as deformation degree continues to increase, dynamic softening and work hardening reach a dynamic equilibrium, resulting in a stable flow stress[27–28].

The peak stress for the studied alloy is shown in Fig.5. For various deformation parameters, the variation trend of the peak stress shows a certain regularity. At constant temperature, the peak stress increases as strain rate increases. At low strain rate, the recrystallized grains have enough time for nucleation and growth, resulting in a more fully formed DRX[29]. When the strain rate remains unchanged, as the temperature increases, the atoms are more likely to migrate and diffuse, thereby reducing the cross-slip resistance and deformation resistance of the dislocation, which ultimately leads to a decrease in the peak stress[30]. Therefore, the softening behavior occurs more easily at lower strain rates and higher temperatures.

3.2 Microstructure evolution

Fig.6 and Fig.7 show EBSD inverse pole figures (IPFs) and grain size distributions under different deformation parameters, respectively. Fig. 6a illustrates that the original grain becomes flat along the compression direction with few fine DRX grains appearing in deformed grains. Meanwhile, some twin structures can also be observed. The original grain boundary undulates into the interior of adjacent grains in Fig.6b–6c and 6e. When the deformation condition is 1050 °C/ 1 s^{-1} (Fig.6c), the originally straight grain boundaries between adjacent grains bow out to form a serrated shape (as shown in the white circles). These positions (as shown in the white circles) can be considered as the nucleation sites of DRX grains. As is well known, the formation of DRX is followed by nucleation and growth of new grains. The primary cause of DRX nucleation is the difference in dislocation density. The difference in dislocation density causes a difference in local stored energy. The phenomenon of grain boundary bowing

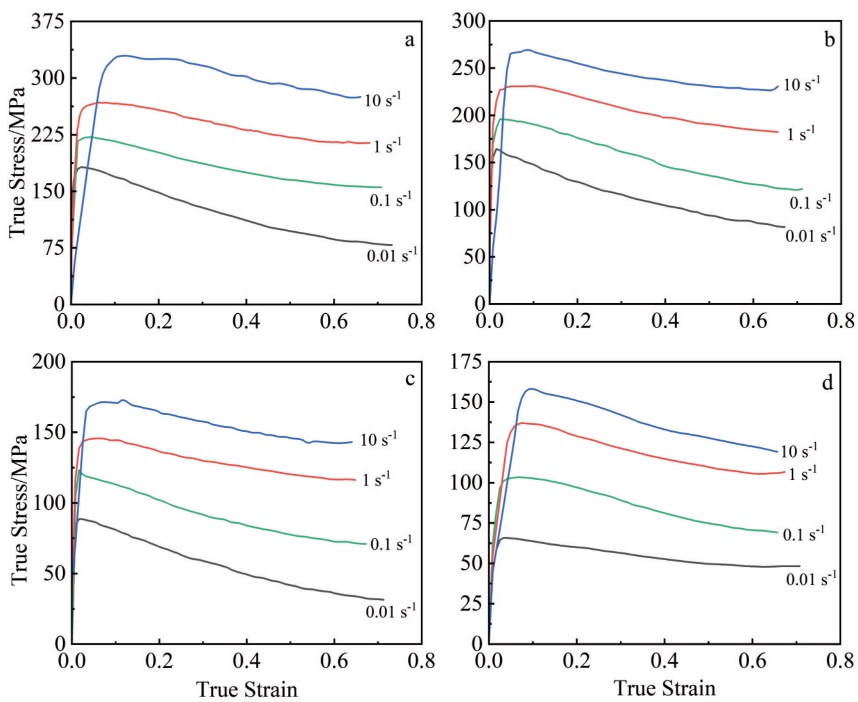

Fig.4 True stress-true strain curves of Fe-Cr-Ni-based alloys at different temperatures: (a) 950 °C; (b) 1000 °C; (c) 1050 °C; (d) 1100 °C

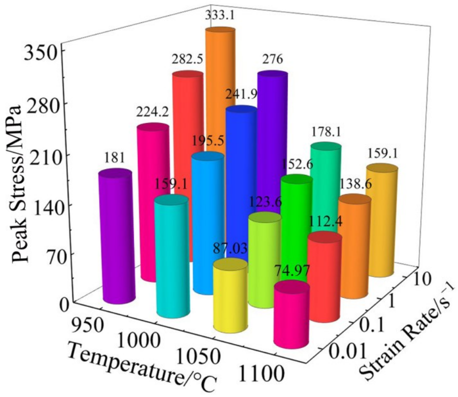

Fig.5 Peak stress of Fe-Cr-Ni-based alloys under different deformation conditions

occurs when an area with low dislocation density grows into adjacent grains with high dislocation density. This mechanism is denoted as grain boundary bowing nucleation. Fig. 6f illustrates that the grain entirely consists of DRX grains with uniform grain size and straight grain boundaries.

Fig. 6a – 6b and 6d – 6e indicate that grain refinement is obvious as strain rate decreases due to the occurrence of DRX. When the strain rate is low, it is easy to form substructures and release deformation energy rapidly through nucleation and growth of DRX. The substructure cannot fully develop as the strain rate increases, and DRX is difficult to nucleate. The grain size becomes finer as the temperature increases, whereas the strain rate remains unchanged. At higher temperatures, atomic thermal vibration becomes more obvious and the diffusion rate increases, allowing dislocations to slip, climb, and cross-slide more easily than at lower temperatures. Meanwhile, higher temperature promotes nucleation of DRX, and the grain boundary migration ability also increases. Thus, at lower temperature and higher strain rate, DRX is less likely to occur. The grain size distributions were obtained by analyzing EBSD images in Fig. 6, as shown in Fig. 7. Under the deformation condition of 1100 °C/0.01 s^{-1}, the grain size is uniform with an average size of around 17 μm, and the grain isometric is good (Fig. 7). At the deformation temperature of 1050 °C and a high strain rate of 1 s^{-1}, the grains with size smaller than 15 μm account for 50%. However, when the strain rate changes to 0.1 s^{-1}, the grains with size smaller than 15 μm account for 45.5%. The grains with size of 15–25 μm account for 33.13% at low strain rate (0.1 s^{-1}) and only 13.77% at high strain rate (1 s^{-1}). When the strain rate is 0.01 s^{-1}, the grains with size less than 15 μm account for 45.35% at high deformation temperature (1100 °C), whereas the grains with size less than 15 μm account for 42.94% and 34.11% at 1000 °C and 950 °C, respectively. Hence, DRX under high deformation temperature and low strain rate is the main mechanism to refine grains of Fe-Cr-Ni-based alloy during hot deformation.

3.3 Model establishment

3.3.1 Arrhenius constitutive model

The Arrhenius constitutive relation suggested by McTegart and Sallars is used in this research to describe the constitutive relation of the studied Fe-Cr-Ni-based alloy[31–32]. The expressions of Arrhenius constitutive relation under different conditions are shown in Eq.(1–3), as follows:

$$\dot{\varepsilon} = A[\sinh(\alpha\sigma)]^n \exp\left(\frac{-Q}{RT}\right) \tag{1}$$

$$\dot{\varepsilon} = A_1 \sigma^{n_1} (\alpha\sigma > 1.2) \tag{2}$$

$$\dot{\varepsilon} = A_2 \exp(\beta\sigma)(\alpha\sigma < 0.8) \tag{3}$$

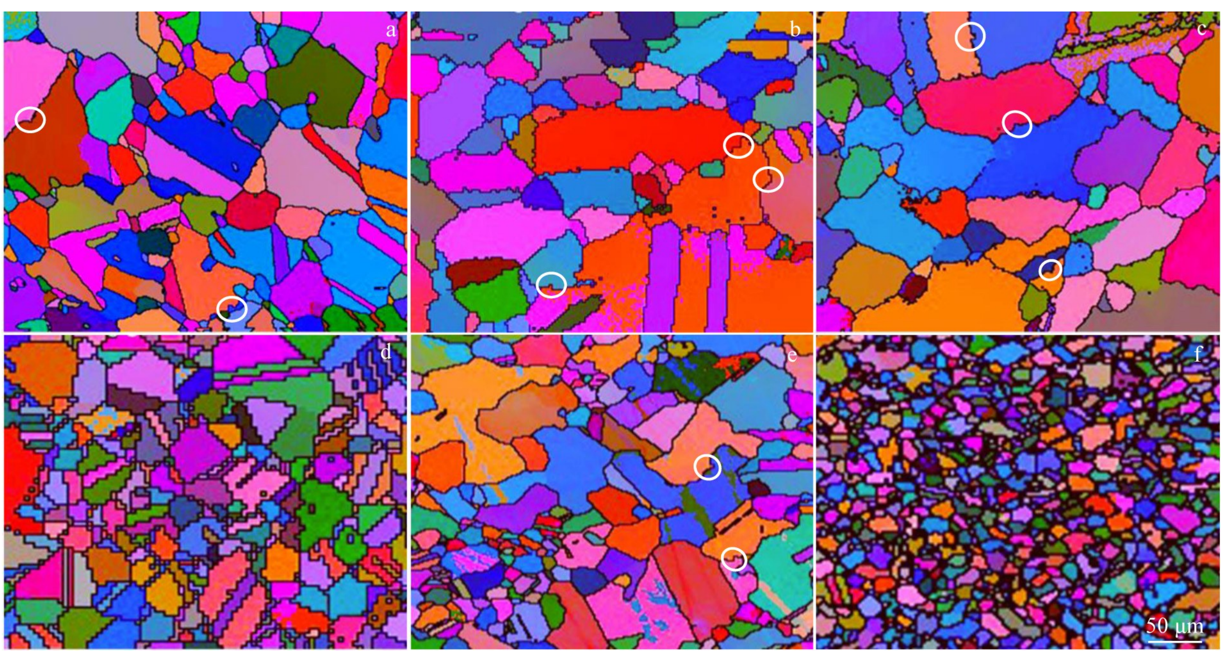

Fig.6 EBSD IPFs of Fe-Cr-Ni-based alloys under different deformation parameters: (a) 1000 °C/0.1 s^{-1}; (b) 1050 °C/1 s^{-1}; (c) 950 °C/0.01 s^{-1}; (d) 1000 °C/0.01 s^{-1}; (e) 1050 °C/0.1 s^{-1}; (f) 1100 °C/0.01 s^{-1}

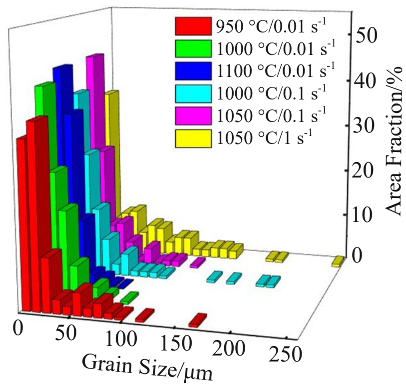

Fig.7 Grain size distributions of Fe-Cr-Ni-based alloys under different deformation parameters

where Q is activation energy for hot deformation (kJ·mol^{-1}); T is temperature; R is gas constant of 8.314 J·mol^{-1}·K^{-1}; $\dot{\varepsilon}$ is strain rate; σ is stress; A, A_1, A_2, α, β, n, and n_1 are material constants[33].

Take natural logarithm of Eq.(1–3) and Eq.(4–6) can be obtained, as follows:

$$\ln\dot{\varepsilon} = \ln A + n\ln[\sinh(\alpha\sigma)] - \frac{Q}{RT} \tag{4}$$

$$\ln\dot{\varepsilon} = \ln A_1 + n_1\ln\sigma \tag{5}$$

$$\ln\dot{\varepsilon} = \ln A_2 + \beta\sigma \tag{6}$$

Generally, a linear relationship exists between steady-state flow stress and peak stress. The relationship between the flow stress and the peak stress is linearly regressed using the peak stress as the flow stress. The values of n_1 and β are solved by the slopes of the fitted lines in Fig. 8a and 8b, respectively. Thus, β=0.0652 and n_1=10.8721. Therefore, α can be obtained:

$$\alpha = \beta/n_1 \tag{7}$$

According to Eq.(7), α=0.006. Substitute the relevant parameters into Eq.(4). The relationship can be obtained, as shown in Fig. 8c. Thus, n=7.8993. Apply the natural logarithm on both sides of Eq.(1), as follows:

$$\ln[\sinh(\alpha\sigma)] = \frac{\ln\dot{\varepsilon}}{n} - \frac{\ln A}{n} + \frac{1000Q}{nRT} \tag{8}$$

A linear relationship exists between ln[sin($\alpha\sigma$)] and 1/T, as shown in Fig. 8d. Take the partial derivative of Eq. (8), as follows:

$$Q = R\left[\frac{\partial\ln\dot{\varepsilon}}{\partial\ln[\sinh(\alpha\sigma)]}\right]_T\left[\frac{\partial\ln[\sinh(\alpha\sigma)]}{\partial(1/T)}\right] \tag{9}$$

The average Q value of the studied Fe-Cr-Ni-based alloy is 807.89 kJ·mol^{-1}.

Generally, Z parameter represents the influence of temperature and strain rate on flow stress[34–35]. Its relationship with flow stress is shown in Eq.(10):

$$Z = \dot{\varepsilon}\exp\left(-\frac{Q}{RT}\right) = A[\sinh(\alpha\sigma)]^n \tag{10}$$

Therefore, Eq. (11) can be obtained from the logarithmic transformation of Eq.(10), as follows:

$$\ln Z = \ln A + n\ln[\sinh(\alpha\sigma)] \tag{11}$$

Eq.(11) can be simplified based on the nature of hyperbolic sinusoid[36], as follows:

$$\sigma = \frac{1}{\alpha}\ln\left\{\left(\frac{Z}{A}\right)^{\frac{1}{n}} + \left[\left(\frac{Z}{A}\right)^{\frac{2}{n}} + 1\right]^{\frac{1}{2}}\right\} \tag{12}$$

Substitute Q and every parameter into Eq. (10), and draw the fitting line of ln$Z$-ln[sinh($\alpha\sigma$)] relationship, as shown in

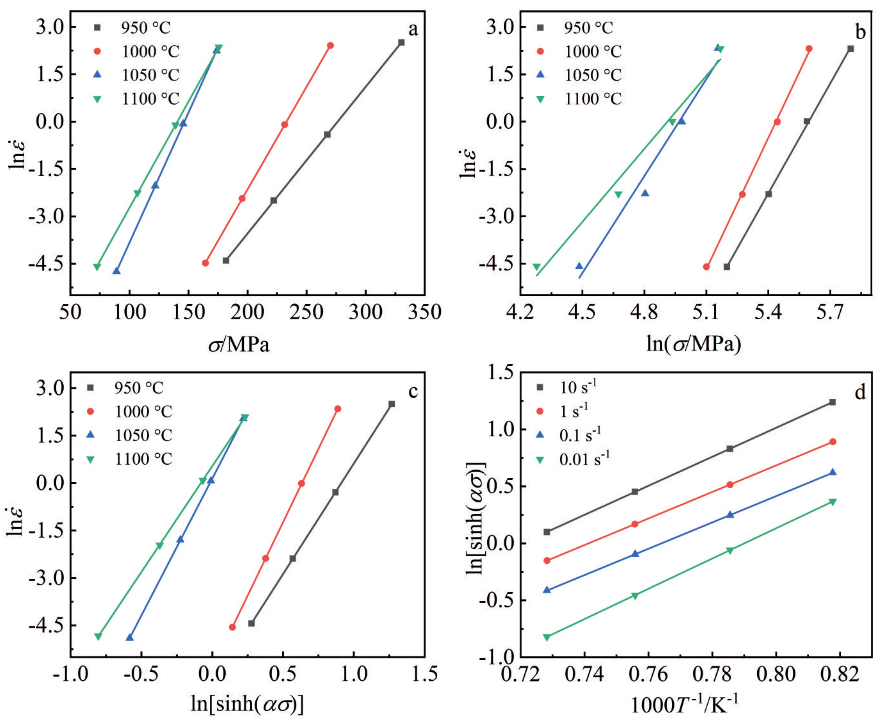

Fig.8 Regression linear curves of Fe-Cr-Ni-based alloys under different deformation conditions: (a) ln$\dot{\varepsilon}$-σ, (b) ln$\dot{\varepsilon}$-lnσ, (c) ln$\dot{\varepsilon}$-ln[sinh($\alpha\sigma$)], and (d) ln[sinh($\alpha\sigma$)]-1000/T

Fig. 9. The linear correlation shows that the Z parameter effectively explains hot deformation characteristics of the studied alloy. In this case, A=2.424×10^{31}.

The Arrhenius constitutive relation is obtained by substituting the material-related parameters A, n, α, and Q into Eq.(1). Thus, Eq.(13) can be obtained, as follows:

$$\dot{\varepsilon} = 2.424 \times 10^{31} [\sinh(0.006\sigma)]^{7.8993} \exp\left(\frac{807890}{RT}\right) \quad (13)$$

The constitutive equation of peak stress can be obtained by substituting n, α, and A into Eq.(12), as follows:

$$\sigma = \frac{1}{0.006} \ln\left\{ \left(\frac{Z}{2.424 \times 10^{31}}\right)^{\frac{1}{7.8993}} + \left[\left(\frac{Z}{2.424 \times 10^{31}}\right)^{\frac{2}{7.8993}} + 1\right]^{\frac{1}{2}} \right\} \quad (14)$$

Thus, the Z parameter is expressed, as follows:

$$Z = \dot{\varepsilon} \exp\left(\frac{807890}{RT}\right) \quad (15)$$

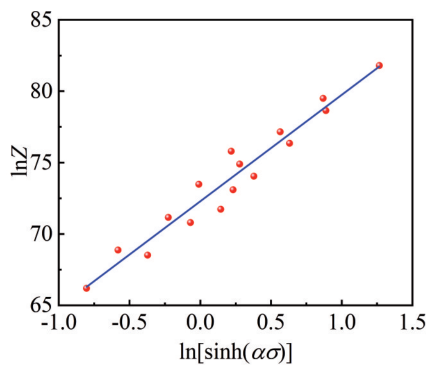

Fig.9 Relationship between ln$Z$ and ln[sinh($\alpha\sigma$)]

3.3.2 Strain-compensated Arrhenius constitutive model

In general, peak stress under different parameters can be predicted by the constitutive model. To precisely forecast flow stress under different deformation stages, it is necessary to take into account the effect of strain on flow stress during the hot deformation. Therefore, an Arrhenius constitutive model with strain compensation was established to accurately predict flow stress of the studied alloy[37].

As is well known, the fifth-order polynomial equation, Eq.(16), can well represent the mathematical relation between material constant and strain[38–39], as follows:

$$\begin{cases} Q(\varepsilon) = Q_0 + Q_1\varepsilon + Q_2\varepsilon^2 + Q_3\varepsilon^3 + Q_4\varepsilon^4 + Q_5\varepsilon^5 \\ \ln A(\varepsilon) = A_0 + A_1\varepsilon + A_2\varepsilon^2 + A_3\varepsilon^3 + A_4\varepsilon^4 + A_5\varepsilon^5 \\ n(\varepsilon) = n_0 + n_1\varepsilon + n_2\varepsilon^2 + n_3\varepsilon^3 + n_4\varepsilon^4 + n_5\varepsilon^5 \\ \alpha(\varepsilon) = \alpha_0 + \alpha_1\varepsilon + \alpha_2\varepsilon^2 + \alpha_3\varepsilon^3 + \alpha_4\varepsilon^4 + \alpha_5\varepsilon^5 \end{cases} \quad (16)$$

Firstly, the values of ln$A$, n, α, and Q with different strains (0.05 – 0.7, interval of 0.05) can be determined by the Arrhenius constitutive model. Fig. 10 displays the fifth-order polynomial function equation that correlates material parameters with strain variables. Table 2 shows the coefficients of this equation.

Data comparison between experimental and predicted values of flow stress is shown in Fig. 11. It can be noticed from Fig. 11 that the predicted values are in high agreement with the experimental values. Fig. 12 shows the relationship between experimental and predicted values obtained from strain-compensated Arrhenius constitutive model with a correlation coefficient of 0.9947. The results indicate that the strain-compensated Arrhenius constitutive model can better predict the flow stress under different

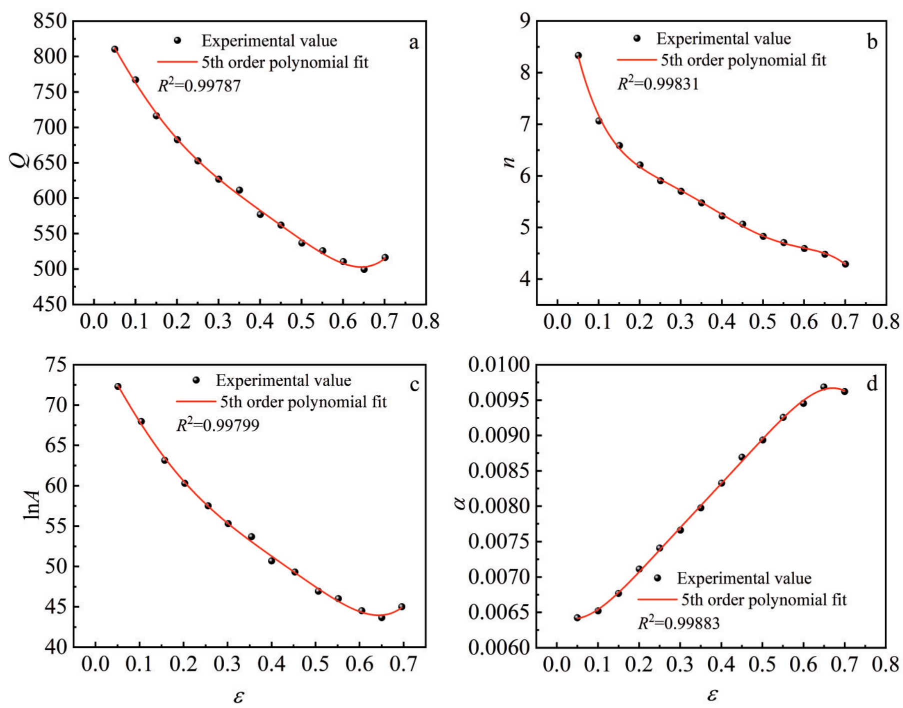

Fig.10 Relationships between material constants of constitutive models and true strain: (a) Q-ε; (b) n-ε; (c) ln$A$-ε; (d) α-ε

Table 2 The fifth-order polynomial equation coefficient of material constants

Degree	$Q/\times10^7$	n	$\ln A$	α
5	1.0059	−423.5022	921.8	−0.1692
4	−1.4154	883.0630	−1282.9	0.3090
3	0.5778	−697.5848	0.5056	−0.2193
2	0.0306	262.3535	42.5	0.0745
1	−0.1107	−51.6536	104.9	−0.0057
0	0.0866	10.3136	77.5	0.0060

deformation stages. Thus, the flow stress at different deformation stages can be predicted from Eq. (17) [33,36,47], as follows:

$$\sigma = \frac{1}{\alpha_{(\varepsilon)}} \ln \left\{ \left(\frac{Z_{[Q(\varepsilon)]}}{A_{(\varepsilon)}} \right)^{\frac{1}{n_{(\varepsilon)}}} + \left[\left(\frac{Z_{[Q(\varepsilon)]}}{A_{(\varepsilon)}} \right)^{\frac{2}{n_{(\varepsilon)}}} + 1 \right]^{\frac{1}{2}} \right\} \tag{17}$$

3.4 Critical conditions for DRX

As is well known, DRX is a significant softening mechanism, which plays an irreplaceable role in improving material properties. During the hot deformation of metal, material dislocation density increases to a specific value, and DRX phenomenon starts to occur in metal material. The corresponding deformation condition is denoted as DRX critical condition[40–41]. The most commonly used method for determining the critical condition is the Poliak-Jonas criterion[42–43]. In this method, work hardening rate (θ=dσ/dε) is determined by solving the true stress-true strain curve, and the relation curve of θ-σ is plotted[44]. The critical point is further obtained by finding the inflection point on the θ-σ curve.

The θ-σ curve of the studied Fe-Cr-Ni-based alloy is presented in Fig. 13. At the beginning, θ slowly declines from the maximum because only DRV exerts softening effect. When DRX reaches the critical condition, the work hardening rate decreases more rapidly due to the combined softening effects of DRX and DRV. The critical point of DRX is reflected by the inflection point of θ-σ curve, but sometimes the inflection point is not obvious. To obtain the inflection point more accurately, the partial derivative of θ-σ curve is solved[45]. Fig. 14 shows that the $-\partial\theta/\partial\sigma$-$\sigma$ curves decrease firstly and then increase, and the lowest points correspond to DRX critical points of the studied Fe-Cr-Ni-based alloy[46].

Fig. 15 shows a three-dimensional histogram of DRX critical stresses. The critical stress increases as the temperature decreases or the strain rate increases. Under the condition of high temperature and low strain rate, high temperature provides enough energy for diffusion of the vacancy atoms and dislocation movement, and low strain rate provides enough time for dislocations to move or rearrange, resulting in more adequate nucleation and growth of DRX. With higher strain rates, the rapid proliferation and winding of dislocations lead to dislocation accumulation, resulting in stress concentration, which restricts DRX formation.

Fig. 16 illustrates linear fitting relationship between critical stress (strain) and peak stress (strain), and fitting results show a linear relationship, as follows:

$$\begin{cases} \sigma_c = 0.8983\sigma_p \\ \varepsilon_c = 0.3858\varepsilon_p \end{cases} \tag{18}$$

where σ_p and σ_c are peak stress and critical stress, respectively; ε_p and ε_c are peak strain and critical strain, respectively.

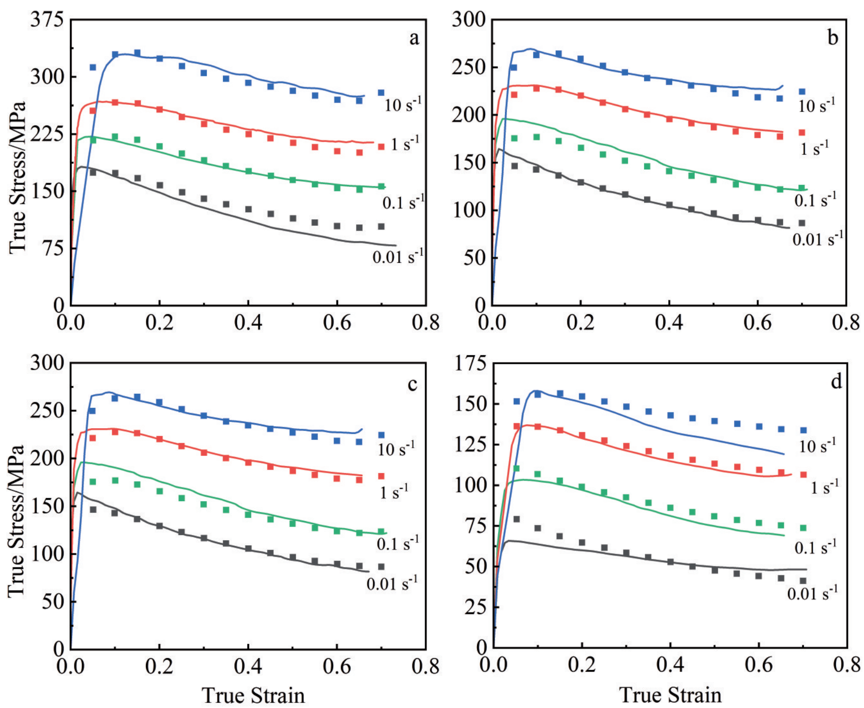

Fig.11 Correlation between experimental and predicted values of flow stress at different temperatures: (a) 950 °C; (b) 1000 °C; (c) 1050 °C; (d) 1100 °C

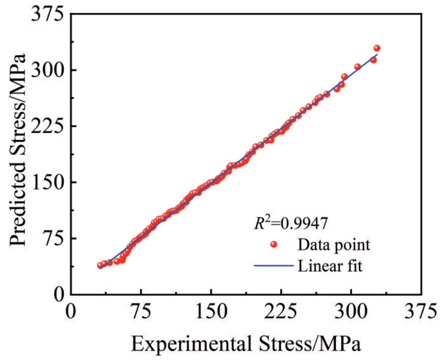

Fig.12 Comparison between predicted and experimental values of flow stress

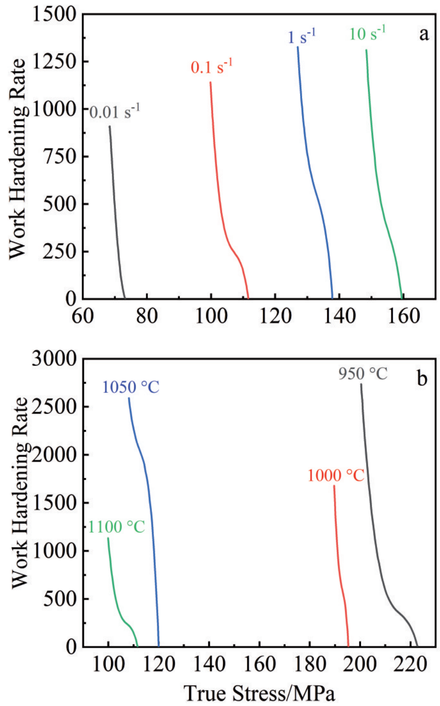

Fig.13 Relationship between work hardening rate and true stress at different deformation conditions: (a) constant temperature of 1100 °C; (b) constant strain rate of 0.1 s^{-1}

Fig. 17 shows the linear relationship between Z parameter and critical condition of DRX, and Eq.(19) can be obtained through linear fitting, as follows:

$$\begin{cases} \sigma_c = 0.2321Z^{0.0881} \\ \varepsilon_c = 0.00192Z^{0.064} \end{cases} \tag{19}$$

Combined with Fig.17 and Eq.(19), it can be seen that the decrease in Z value results in a decrease in critical stress, promoting the occurrence of DRX. Grain boundary migration and growth have sufficient energy and time at low Z condition (high temperature or low strain rate). In Fig.6d and 6f, with a small Z value, grains are refined, and the degree of recrystallization is higher. The migration of dislocation and grain boundary is fast, and DRX is more easily to occur. Fig.6a–6b show that the softening effect is not significant at high Z condition

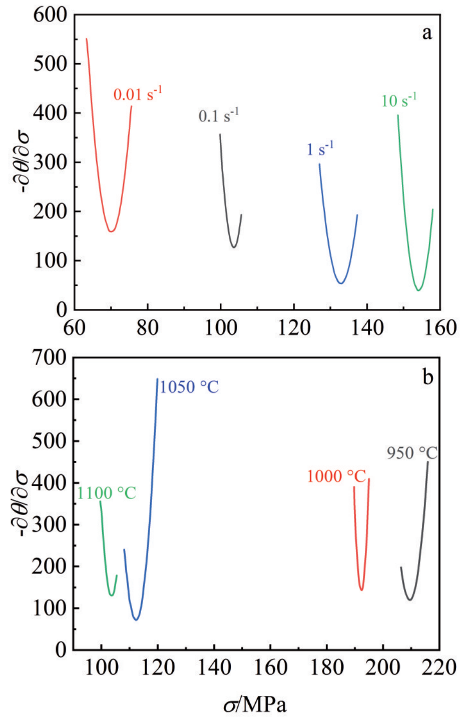

Fig.14 Relationship between $-\partial\theta/\partial\sigma$ and σ at different deformation conditions: (a) constant temperature of 1100 °C; (b) constant strain rate of 0.1 s^{-1}

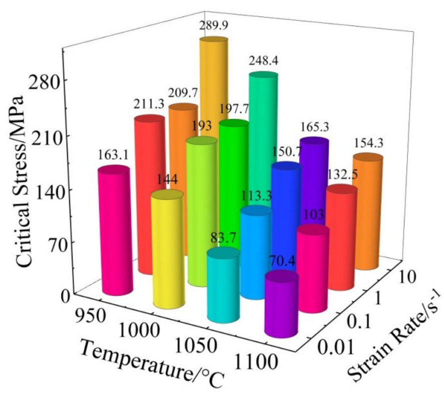

Fig.15 Critical stress under different deformation conditions

(high strain rate or low temperature). The higher strain rate results in continuous dislocation accumulation, which is not conducive to DRX. The stress concentration at the grain boundary results from intensification of interaction between dislocations and that between dislocations and grain boundary.

3.5 Modeling of DRX kinetics

The softening effect of DRX during hot deformation is very effective for removing defects and improving material properties. Researchers have studied DRX behavior of metal materials during hot deformation by constructing DRX kinetic models[47–48]. In this research, the Avrami model was used to construct DRX kinetic model[49]. Its model expression is displayed in Eq.(20), as follows:

$$X = 1 - \exp\left[-k\left(\frac{\varepsilon - \varepsilon_c}{\varepsilon_p}\right)^m\right] \tag{20}$$

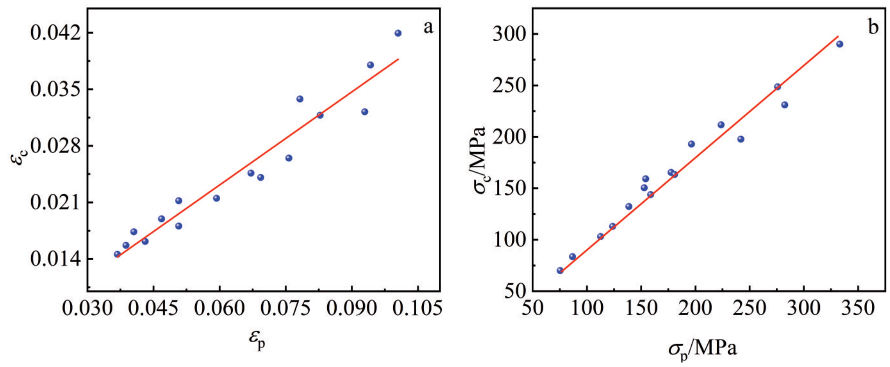

Fig.16 Linear relationships of ε_c-ε_p (a) and σ_c-σ_p (b)

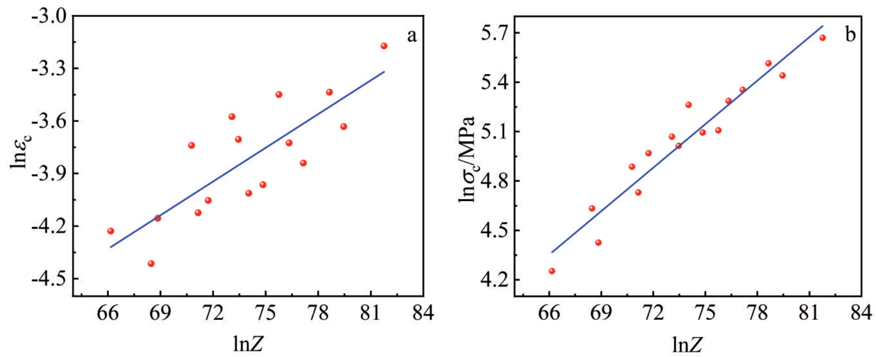

Fig.17 Linear relationships of lnε_c-ln$Z$ (a) and lnσ_c-ln$Z$ (b)

where m and k are material constants. Obtaining DRX volume fraction is a prerequisite for constructing an Avrami model. Therefore, the stress-softening model was employed to obtain DRX volume fraction[49], as follows:

$$X = \frac{\sigma_p - \sigma}{\sigma_p - \sigma_s} \tag{21}$$

where σ_s is softening stress when DRX occurs and reaches a stable state[50].

The logarithm of Eq.(20) can be obtained, as follows:

$$\ln\ln\left(\frac{1}{1 - X}\right) = m\ln\left(\frac{\varepsilon - \varepsilon_c}{\varepsilon_p}\right) + \ln k \tag{22}$$

where X is the DRX content (vol%).

Fig. 18 shows the linear fitting results of $\ln[\ln(1-X)^{-1}]$ and $\ln[(\varepsilon-\varepsilon_c)/\varepsilon_p]$ at different strain rates. At the strain rate of 0.1 s^{-1}, the fitting line indicates that m=1.4478 and k=0.062; at the strain rate of 0.01 s^{-1}, m=1.6559 and k=0.0469. Therefore, DRX content can be derived from Eq.(23–24) when the strain rate is 0.1 and 0.01 s^{-1}, respectively, as follows:

$$X = 1 - \exp\left[-0.062\left(\frac{\varepsilon - \varepsilon_c}{\varepsilon_p}\right)^{1.4478}\right] \tag{23}$$

$$X = 1 - \exp\left[-0.047\left(\frac{\varepsilon - \varepsilon_c}{\varepsilon_p}\right)^{1.6559}\right] \tag{24}$$

Fig. 19 shows the relationships between DRX content and true strain. The change trend of DRX content presents a typical S-type curve, indicating that DRX content is decreased with the decrease in temperature or the increase in strain rate. The temperature rise enhances the ability of nucleation and dislocation migration at grain boundaries, accelerating the

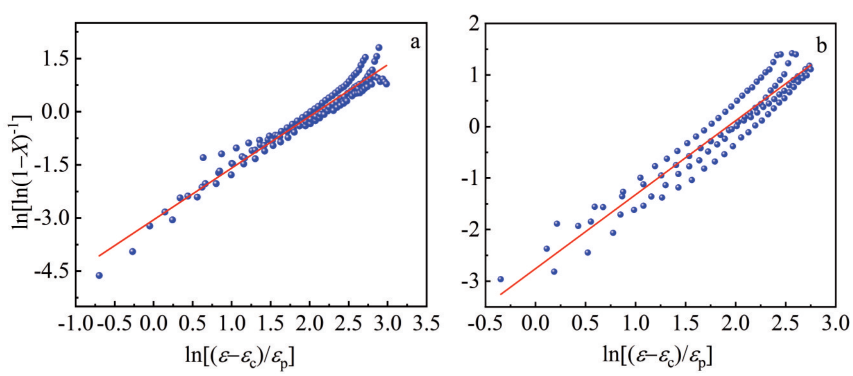

Fig.18 Linear relationships between $\ln[\ln(1-X)^{-1}]$ and $\ln[(\varepsilon-\varepsilon_c)/\varepsilon_p]$ at strain rate of 0.01 s^{-1} (a) and 0.1 s^{-1} (b)

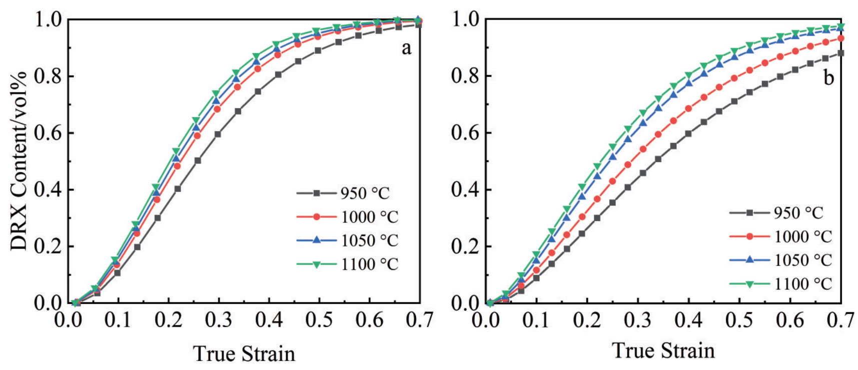

Fig.19 Relationships between DRX content and true strain at strain rate of 0.01 s^{-1} (a) and 0.1 s^{-1} (b)

formation of DRX. Due to the decrease in strain rate, recrystallization can form and grow sufficiently, thus increasing the DRX content. Therefore, the occurrence of DRX can be controlled by adjusting the deformation parameters to improve microstructure and properties.

4 Conclusions

1) According to the true stress-true strain curves, the studied Fe-Cr-Ni-based alloy exhibits typical dynamic softening phenomenon. EBSD IPF indicates that hot deformation process can generate DRX and its main nucleation mechanism is grain boundary bowing nucleation.

2) The strain-compensated Arrhenius constitutive model is constructed. The correlation coefficient (R) between the experimental and predicted values is 0.9947, suggesting that the developed model can accurately predict flow stress. The model equation is as follows:

$$\sigma = \frac{1}{0.006}\ln\left\{\left(\frac{Z}{2.424\times10^{31}}\right)^{\frac{1}{7.8993}} + \left[\left(\frac{Z}{2.424\times10^{31}}\right)^{\frac{2}{7.8993}} + 1\right]^{\frac{1}{2}}\right\}$$

3) The critical values of DRX are obtained from the θ-σ curves, and the Z parameter is introduced to describe the critical condition of DRX. The relationship between the critical eigenvalues and the Z parameters is as follows:

$$\begin{cases} \sigma_c = 0.8983\sigma_p \\ \varepsilon_c = 0.3858\varepsilon_p \\ \sigma_c = 0.2321Z^{0.0881} \\ \varepsilon_c = 0.00192Z^{0.064} \end{cases}$$

4) The DRX kinetic model is constructed using the Avrami model, and a typical S-type curve is obtained. The kinetic model for DRX can well predict the DRX content, as follows:

$$\begin{cases} X = 1 - \exp\left[-0.062\left(\frac{\varepsilon-\varepsilon_c}{\varepsilon_p}\right)^{1.4478}\right] & \dot{\varepsilon} = 0.1\ s^{-1} \\ X = 1 - \exp\left[-0.047\left(\frac{\varepsilon-\varepsilon_c}{\varepsilon_p}\right)^{1.6559}\right] & \dot{\varepsilon} = 0.01\ s^{-1} \end{cases}$$

References

1 Li Ang, Wu Fu, Gao Wei *et al. Rare Metal Materials and Engineering*[J], 2021, 50(2): 531 (in Chinese)

2 Nian V. *Progress in Nuclear Energy*[J], 2018, 105: 83

3 Xin J J, Song Y T, Fang C *et al. Fusion Engineering and Design*[J], 2018, 133: 70

4 Ye C, Lu G, Peng X *et al. Proceedings of the Institution of Mechanical Engineers, Part C: Journal of Mechanical Engineering Science*[J], 2020, 234: 4258

5 Ferreira R P, Nascimento C C F, Reis G S *et al. Materials Sciences and Applications*[J], 2020, 11: 217

6 Kumar T S, Yadav S D, Nagesha A *et al. Materials Science and Engineering A*[J], 2020, 772: 138627

7 Chen X D, Chen Y F, Shi Y Z *et al. Annals of Nuclear Energy*[J], 2018, 120: 835

8 Momeni A, Dehghani K. *Materials Science and Engineering A*[J], 2011, 528: 1448

9 Zhang C, Zhang L W, Shen W F *et al. Materials & Design*[J], 2016, 90: 804

10 Ding Wanwu, Chen Shihao, Hu Liwen *et al. Rare Metal Materials and Engineering*[J], 2023, 52(12): 4086

11 Wang Chenchong, Wei Xiaolu, Shen Chunguang *et al. Materials China*[J], 2019, 38(7): 663 (in Chinese)

12 Wu Zhiqiang, Deng Siying, Liu Huan *et al. Rare Metal Materials and Engineering*[J], 2022, 51(7): 2599 (in Chinese)

13 Jafari M, Najafizadeh A. *Materials Science and Engineering A*[J], 2009, 501: 16

14 Xiong Y B, Wen D X, Li J J *et al. Metals and Materials International*[J], 2021, 27: 3945

15 Wang Fa, Jiang He, Dong Jianxin. *Rare Metal Materials and Engineering*[J], 2023, 52(1): 245 (in Chinese)

16 Zhang Haiyan, Cheng Ming, Hu Rufu *et al. Rare Metal Materials and Engineering*[J], 2023, 52(11): 3778

17 Chiu C H, Wu H Y, Wu C T. *Applied Mechanics and Materials*[J], 2013, 378: 178

18 Jin M, Lu B, Liu X G *et al. Journal of Iron and Steel Research International*[J], 2013, 20: 67

19 Li C, Huang L, Zhao M *et al. Materials Science and Engineering A*[J], 2020, 797: 139925

20 Li Nana, Liu Jianglin, Zhang Wei *et al. Rare Metal Materials and Engineering*[J], 2020, 49(8): 2712 (in Chinese)

21 Zhang W, Zhang J, Han Y *et al. Journal of Iron and Steel

Research International[J], 2016, 23(2): 151
22 Zhao H, Qi J, Su R *et al*. *Journal of Materials Research and Technology*[J], 2020, 9: 2856
23 Chegini M, Aboutalebi M R, Seyedein S H *et al*. *Journal of Manufacturing Processes*[J], 2020, 56: 916
24 Li B, Yang H, Chu Z J *et al*. *Journal of Materials Engineering and Performance*[J], 2023, 33(14): 7195
25 Liu L, Wu Y X, Gong H *et al*. *Journal of Alloys and Compounds*[J], 2020, 817: 153301
26 Liu J, Wang X H, Liu J T *et al*. *Journal of Alloys and Compounds*[J], 2019, 782: 224
27 Yao Jingjing, Zhang Di, Zhang Jishan. *Rare Metal Materials and Engineering*[J], 2022, 51(6): 2046
28 Chen M S, Yuan W Q, Li H B *et al*. *Materials Characterization*[J], 2019, 147: 173
29 Zong Y Y, Shan D B, Xu M *et al*. *Journal of Materials Processing Technology*[J], 2009, 209: 1988
30 Zhai R X, Wang W, Ma R *et al*. *Journal of Materials Engineering and Performance*[J], 2020, 29: 964
31 Wu Jinjian, Zhao Guangdi, Wang Bo *et al*. *Materials China*[J], 2024, 43(10): 902 (in Chinese)
32 Ding S, Khan S A, Yanagimoto J. *Materials Science and Engineering A*[J], 2020, 787: 139522
33 Lu D D, Li J F, Guo Y J *et al*. *Metals and Materials International*[J], 2023, 29(6): 1652
34 Wang X, Zhang Y, Ma X. *Materials Science and Engineering A*[J], 2020, 778: 139077
35 He H L, Yi Y P, Cui J D *et al*. *Vacuum*[J], 2019, 60: 293
36 Liu Shuang, Feng Jing, Luo Xi *et al*. *Rare Metal Materials and Engineering*[J], 2022, 51(8): 2850
37 Lu Y, Xie H, Wang J *et al*. *Vacuum*[J], 2021, 186: 110066
38 Cai Zhen, Wu Tiandong, Wei Na *et al*. *Rare Metal Materials and Engineering*[J], 2022, 51(11): 4051
39 Cai Z, Ji H C, Pei W C *et al*. *Vacuum*[J], 2019, 165: 324
40 Wang Xingmao, Ding Yutian, Gao Yubi *et al*. *Rare Metal Materials and Engineering*[J], 2022, 51(1): 249 (in Chinese)
41 Li B, Chu Z J, Du Y *et al*. *Journal of Materials Engineering and Performance*[J], 2020, 29: 7774
42 Poliak E I, Jonas J J. *Acta Materialia*[J], 1996, 44: 127
43 Poliak E I, Jonas J J. *ISIJ International*[J], 2003, 43(5): 692
44 Han Y, Yan S, Yin B G *et al*. *Vacuum*[J], 2018, 148: 78
45 Lu Y, Xie H B, Wang J *et al*. *Vacuum*[J], 2021, 186: 110066
46 Liu X G, Zhang L G, Qi R S *et al*. *Journal of Iron and Steel Research International*[J], 2016, 23: 238
47 Chu Zhaojie, Li Bo, Wang Wenhao *et al*. *Rare Metal Materials and Engineering*[J], 2021, 50(7): 2502 (in Chinese)
48 Geng Y F, Li X, Zhang Y *et al*. *Vacuum*[J], 2020, 177: 109376
49 Luo R, Chen L L, Zhang Y X *et al*. *Journal of Alloys and Compounds*[J], 2021, 865: 158601
50 Zhang C S, Wang C X, Guo R *et al*. *Journal of Alloys and Compounds*[J], 2019, 773: 59

核电站用Fe-Cr-Ni基合金热变形特征

杨　涵[1,2]，李　波[1,2]，鲁金伟[1,2]，许　龙[1,2]，陈万庆[2,3]，周　炜[4]，杜　勇[5]

(1. 三峡大学 石墨增材制造技术与装备湖北省工程研究中心，湖北 宜昌 443002)

(2. 三峡大学 机械与动力工程学院，湖北 宜昌 443002)

(3. 广东美的集团厨卫电器制造有限公司，广东 佛山 528311)

(4. 西北工业大学 材料学院，陕西 西安 710072)

(5. 中南大学 粉末冶金国家重点实验室，湖南 长沙 410083)

摘　要：采用Gleeble-3500热模拟试验机研究了核电站用Fe-Cr-Ni基合金热变形特征。利用电子背散射衍射（EBSD）技术研究了合金热变形微观组织演化规律。结果表明：流变应力曲线表现出典型的动态再结晶（DRX）特征。EBSD分析发现，DRX晶粒主要在晶界处形核长大。在1100 ℃/0.01 s^{-1}条件下发生完全DRX，晶粒明显细化。合金的主要形核机制是晶界弯曲形核。因此，核电站用Fe-Cr-Ni基合金的软化机制是动态恢复和DRX的结合。建立了具有应变补偿的Arrhenius本构模型。预测值与实验值的相关系数为0.9947。得到了临界应力（应变）和Z参数的可靠数学模型。DRX的临界应力（应变）随温度的降低或应变速率的增大而增大。通过Avrami模型建立了DRX动力学模型，并得到了典型的S型曲线。随着应变速率的降低和温度的升高，DRX的体积分数增加。

关键词：Fe-Cr-Ni基合金；EBSD；本构方程；DRX

作者简介：杨　涵，女，1997年生，硕士生，三峡大学机械与动力工程学院，湖北 宜昌 443002，E-mail：yanghan@ctgu.edu.cn